# Gravitationally lensed galaxies at $2 < z < 3.5$: direct abundance measurements of Lyα emitters$^\star$

Lise Christensen,[1]† Peter Laursen,[1,2] Johan Richard,[1,3] Jens Hjorth,[1]
Bo Milvang-Jensen,[1] Miroslava Dessauges-Zavadsky,[4] Marceau Limousin,[5]
Claudio Grillo[1] and Harald Ebeling[6]

[1]*Dark Cosmology Centre, Niels Bohr Institute, University of Copenhagen, Juliane Maries Vej 30, 2100 Copenhagen, Denmark*
[2]*Oskar Klein Centre, Department of Astronomy, Stockholm University, SE-10691 AlbaNova, Stockholm, Sweden*
[3]*Centre de Recherche Astrophysique de Lyon, Université Lyon 1, Observatoire de Lyon, 9 Avenue Charles André, 69561 Saint Genis Laval cedex, France*
[4]*Observatoire de Genève, Université de Genève, 51 Ch. des Maillettes, 1290 Sauverny, Switzerland*
[5]*Aix Marseille Université, CNRS, LAM (Laboratoire d'Astrophysique de Marseille) UMR 7326, 13388 Marseille, France*
[6]*Institute for Astronomy, University of Hawaii, 2680 Woodlawn Drive, Honolulu, HI 96822, USA*

## ABSTRACT

Strong gravitational lensing magnifies the flux from distant galaxies, allowing us to detect emission lines that would otherwise fall below the detection threshold for medium-resolution spectroscopy. Here we present the detection of temperature-sensitive oxygen emission lines from three galaxies at $2 \lesssim z \lesssim 3.5$, which enables us to directly determine the oxygen abundances and thereby double the number of galaxies at $z > 2$ for which this has been possible. The three galaxies have ∼10 per cent solar oxygen abundances in agreement with strong emission-line diagnostics. Carbon and nitrogen ratios relative to oxygen are subsolar as expected for young metal-poor galaxies. Two of the galaxies are Lyman α (Lyα) emitters with rest-frame equivalent widths of 20 and 40 Å, respectively, and their high magnification factors allow us for the first time to gain insight into the physical characteristics of high-redshift Lyα emitters. Using constraints from the physical properties of the galaxies, we accurately reproduce their line profiles with radiative transfer models. The models show a relatively small outflow in agreement with the observed small velocity offsets between nebular emission and interstellar absorption lines.

**Key words:** gravitational lensing: strong – galaxies: abundances – galaxies: evolution – galaxies: high-redshift.

## 1 INTRODUCTION

Strong gravitational lensing of distant galaxies behind massive galaxy clusters allows us to study intrinsically fainter galaxies than possible for regular field galaxies. With magnification factors reaching up to 50, it becomes possible to study the detailed physical properties of galaxies that are fainter than the characteristic luminosity, $L^*$, at a given redshift. Since the first detailed analyses of a lensed Lyman break galaxy (LBG), MS 1512-cB58 (Pettini et al. 2000, 2002; Teplitz et al. 2000), a steady increase in the number

of spectroscopic observations of bright galaxies at $z \sim 2$ either detected serendipitously or in large dedicated surveys have appeared (e.g. Fosbury et al. 2003; Cabanac et al. 2005; Allam et al. 2007; Swinbank et al. 2007; Stark et al. 2008; Diehl et al. 2009; Hainline et al. 2009; Lin et al. 2009; Bian et al. 2010; Rigby et al. 2011). To date, most lensed galaxies that have received more attention still belong to the bright end of the luminosity function, although recent investigations have started to probe the lower mass end of the galaxy distribution (Richard et al. 2011; Wuyts et al. 2012). Some galaxies show particularly strong ultraviolet (UV) emission lines, suggesting the presence of a large population of very massive, hot stars (Fosbury et al. 2003; Villar-Martín, Cerviño & González Delgado 2004; Raiter, Fosbury & Teimoorinia 2010), giving rise to nebular emission lines that are very rarely detected in nearby galaxies. Other strongly star-forming lensed galaxies have UV spectra that do not differ substantially from the cB58 galaxy spectrum (Quider et al. 2009, 2010; Dessauges-Zavadsky et al. 2010, 2011).

With the boost of the fluxes from gravitational lensing, it also becomes feasible to detect emission lines such as [O III] $\lambda 4363$ or [N III] $\lambda 5755$ which, when related to other transitions from the same ionization stage, are sensitive to the gas temperature. Combining this with the knowledge of the density of the gas, it is possible to derive the abundances of various chemical elements directly (Osterbrock 1989). This approach is widely used to determine abundances in low-redshift galaxies. The flux from the [O III] $\lambda 4363$ line increases with decreasing metallicity; however, low-metallicity galaxies at high redshift are also very faint, so the line is difficult to detect, in particular since the line is redshifted to near-infrared (IR) part of the spectrum. The high-redshift LBGs with <25.5 mag (Steidel et al. 1996) are known to be massive galaxies, and because of the relation between mass and metallicity, LBGs are typically metal rich (Erb et al. 2006). This implies that their temperature-sensitive lines have fluxes below the detection threshold even on the largest telescopes. To date, only one detection of [O III] $\lambda 4363$ from a galaxy at $z > 1$ has been reported (Yuan & Kewley 2009), while other attempts to measure the line have led to upper limits only (Rigby et al. 2011). Analysing other rest-frame UV lines (O III] $\lambda\lambda 1661$, 1666), which are also sensitive to the gas temperature may alleviate this difficulty of detecting [O III] $\lambda 4363$ and determining abundances directly (Villar-Martín et al. 2004; Erb et al. 2010). However, this doublet is also rarely observed in high-redshift galaxies, and it is more sensitive to uncertainties in the correction of extinction in the UV range of the spectrum.

To avoid the need for very long observation times to detect the temperature sensitive lines, alternative methods have been developed. Using only strong rest-frame optical emission lines, various diagnostics have been calibrated with respect to the direct abundance determinations (e.g., Pagel et al. 1979; Pettini & Pagel 2004; Kewley & Ellison 2008). Since the temperature-sensitive lines are generally too weak to be measured even in bright emission-line galaxies at high redshifts, we are forced to use the relations established at low redshifts to derive abundances. The validity of using the exact same strong-line diagnostics at high redshifts has to be verified.

To find potential UV bright high-redshift galaxies, we have studied a sample of gravitationally lensed galaxies at $1 < z < 6$, based on selecting high surface brightness regions in extended arcs. In a companion paper (Christensen et al. 2012, hereafter Paper I), we present the sample and the continuum emission properties of the galaxies. We determine stellar masses from spectral fitting, star formation rates (SFRs) from emission lines and oxygen abundances. We also demonstrate that the low-mass galaxies exhibit a large scatter compared to the fundamental relation for star-forming galaxies (Lara-López et al. 2010; Mannucci et al. 2010) and provide an alternative calibration valid for low-mass galaxies.

Out of the 12 galaxies in our original sample, three galaxies at $1.8 < z < 3.5$ show temperature-sensitive lines. Two of these are also strong Lyman $\alpha$ (Ly$\alpha$) emitters, while the third galaxy shows Ly$\alpha$ in absorption. In this paper we present a more detailed analysis of the nebular emission lines from these three galaxies. We present the data in Section 2, and derive the direct abundances and determine escape fractions in Section 3. In Section 4 we model the two Ly$\alpha$ emission lines using constraints from the physical properties of the galaxies.

## 2 OBSERVATIONAL DATA

The data for the lensed galaxies were obtained with X-shooter on the Very Large Telescope (VLT) during separate observing runs in 2010–2011. One of the science drivers for X-shooter (D'Odorico et al. 2006; Vernet et al. 2011) is to determine redshifts of faint single targets and analyse emission-line galaxies at $z > 1$. In previous papers, we demonstrated the ability of X-shooter for the observations of lensed galaxies (Christensen et al. 2010; Dessauges-Zavadsky et al. 2010; Pettini et al. 2010). In Paper I, we describe the target selection, observations, data reduction and analysis of the spectra. In this paper, we focus on the analysis of the final emission-line fluxes from three galaxies after correcting for many effects: Galactic extinction, intrinsic extinction, slit losses and lens magnification. One of the lensed galaxies is found in the well-studied Abell 1689 cluster, while the remaining two are found in two southern equivalents to the Massive Cluster Survey (MACS) clusters (Ebeling, Edge & Henry 2001) with declinations $< -40°$ (Ebeling, unpublished). This section presents the three galaxies which we can investigate in further detail.

### 2.1 Abell 1689 arc ID 31.1

The arc ID 31.1 is adopted from Limousin et al. (2007). For this target, a wealth of emission lines are observed as listed in Table 1. From the strongest emission lines, which are not affected by telluric absorption, and also excluding Ly$\alpha$ we find the redshift $z = 1.8339 \pm 0.0003$. The last column in Table 1 lists the line fluxes after correcting for intrinsic extinction as described in Section 3.1.

The Ly$\alpha$ line profile is double peaked with a much brighter red than blue component, which is the characteristic signature of resonance scattering of photons in an outflowing medium (see Fig. 2). Its rest-frame equivalent width (EW) is 40 Å. In Section 4 we model the line profile taking into account the constraints from physical parameters determined from other emission lines.

We detect the temperature-sensitive [O III] $\lambda 4363$ line. Its strength increases relative to [O III] $\lambda 5007$ with decreasing metallicity, but at high redshifts, the galaxies that have the best signal-to-noise ratio (S/N) spectra are also the brightest and most massive, and hence most metal-rich ones at those redshifts. To date, [O III] $\lambda 4363$ has only been observed in another lensed galaxy at $z = 1.7$, also behind the Abell 1689 cluster (Yuan & Kewley 2009).

**Table 1.** Emission lines from the A1689 31.1 arc.

| Line | $\lambda_r{}^a$ | $\lambda_{obs}$ | $f_{obs}^b$ | $f_{cor}^b$ |
|---|---|---|---|---|
| Ly$\alpha$ | 1215.67 | 3445.77 | 72.7 ± 0.7 | 4309 ± 42 |
| C IV | 1548.20 | 4386.81 | 4.3 ± 0.4 | 137 ± 13 |
| C IV | 1550.77 | 4394.22 | 4.7 ± 0.3 | 149 ± 10 |
| O III] | 1660.81 | 4705.82 | 3.2 ± 0.4 | 90 ± 11 |
| O III] | 1666.15 | 4720.63 | 7.4 ± 0.3 | 206 ± 8 |
| [C III] | 1906.68 | 5402.29 | 9.1 ± 0.4 | 202 ± 9 |
| C III] | 1908.73 | 5408.19 | 4.7 ± 0.4 | 104 ± 9 |
| [O II] | 3727.09 | 10 563.06 | 9.2 ± 0.8 | 68 ± 6 |
| [O II] | 3729.88 | 10 569.40 | 11.7 ± 0.9 | 86 ± 7 |
| [Ne III] | 3869.84 | 10 965.28 | 6.4 ± 2.5 | 44 ± 17 |
| H$\gamma$ | 4341.69 | 12 301.90 | 17.0 ± 2.1 | 97 ± 12 |
| [O III] | 4364.44 | 12 366.36 | 6.2 ± 1.8 | 35 ± 10 |
| H$\beta$ | 4862.70 | 13 777.99$^c$ | 42.7 ± 4.9 | 205 ± 24 |
| [O III] | 4960.29 | 14 057.55$^c$ | 63.0 ± 10.6 | 293 ± 49 |
| [O III] | 5008.24 | 14 194.09$^d$ | 211.5 ± 5.7 | 968 ± 26 |

$^a$Rest-frame vacuum wavelengths.
$^b$Emission-line flux in units of $10^{-18}$ erg cm$^{-2}$ s$^{-1}$. $f_{obs}$ and $f_{cor}$ correspond to the observed flux and that corrected for intrinsic reddening, respectively.
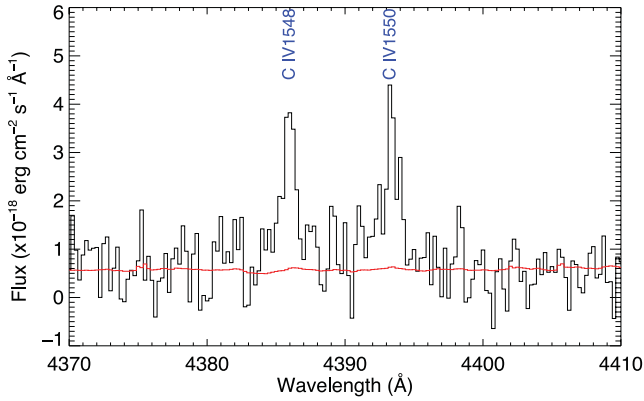$^c$Affected by strong telluric absorption lines.
$^d$Close to sky line.

**Figure 1.** Section of the observed UVB spectrum of the ID 31.1 arc showing its highly uncommon narrow C IV λλ1548, 1550 emission lines. This suggests an ISM with a low covering factor along the line of sight.

Many other rest-frame UV emission lines are identified in the Abell 1689 ID 31.1 spectrum. In particular we draw attention to the narrow emission lines from the C IV λλ1548, 1550 doublet shown in Fig. 1. C IV λλ1548, 1550 are almost always seen in absorption in high-redshift galaxies (another exception is the Lynx arc in Holden et al. 2001; Fosbury et al. 2003), or in P Cygni profiles with a minor contribution from the emission component compared to the absorption (Pettini et al. 2000). This indicates a highly unobscured line of sight to the galaxy. Searching for the UV absorption lines in the low S/N spectrum, we only detect weakly the Si II λλ1260, 1264 and 1526 lines at $z = 1.8348 \pm 0.0012$, while we do not detect the typically strong high-ionization absorption doublet Si IV λλ1393, 1402. Because of the weak absorption lines, we argue that the interstellar medium (ISM) only has a partial coverage, like observed for a couple of other lensed galaxies (Quider et al. 2009; Dessauges-Zavadsky et al. 2010). Among the uncommon emission lines, we also detect the temperature-sensitive O III] λλ1661, 1666 lines, which among other high-$z$ galaxies are also observed in the bright $z = 2.3$ galaxy Q2343–BX418 (Erb et al. 2010) and in the Lynx arc (Fosbury et al. 2003; Villar-Martín et al. 2004).

## 2.2 SMACS J0304.3−4402 ID 1.1

The X-shooter spectrum covers one of the multiple lensed images, and within the slit three distinct regions are visible in the *Hubble Space Telescope* (*HST*) image (see Paper I). The emission lines listed in Table 2 present a sum of the total flux from the components within the slit. The redshift for this galaxy is measured to be $z = 1.9634 \pm 0.0002$. Again, we detect the O III] λλ1661, 1666 doublet. Apart from velocity offsets of ∼100 km s$^{-1}$ between emission lines from the two components, there are no significant differences in the relative line fluxes as verified by comparing extracted spectra from the two distinct component. The UV continuum has the same flux, but redwards of 2600 Å in the rest frame, the continuum emission differs by a factor of 2, with the smallest flux coming from the most compact component. The emission-line fluxes listed in Table 2 are the total flux in the X-shooter slit summed for the two components. Even though the Balmer lines are very bright for this source, Lyα emission is absent, and its (UV) spectrum appears similar to the cB58 spectrum (Pettini et al. 2000).

In addition to the strong UV absorption lines in the ISM, a strong intervening Mg II at $z = 1.5492$ is seen in the visible (VIS) spectrum

**Table 2.** Emission lines from the SMACS J0304 arc.

| Line | $\lambda_{\rm r}$ [a] | $\lambda_{\rm obs}$ | $f_{\rm obs}$ [b] | $f_{\rm cor}$ [b] |
|---|---|---|---|---|
| O III] | 1660.81 | 4921.93 | 7.1 ± 1.6 | 56 ± 13 |
| O III] | 1666.15 | 4937.35 | 11.4 ± 1.9 | 90 ± 15 |
| [O II] | 2470.22 | 7322.39 | 8.4 ± 2.1 | 45 ± 11 |
| [O II] | 3727.09 | 11 044.78 | 437.8 ± 3.4 | 1514 ± 12 |
| [O II] | 3729.88 | 11 053.09 | 587.2 ± 3.9 | 2029 ± 14 |
| H9 | 3836.49 | 11 370.55[c] | 29.1 ± 4.2 | 98 ± 14 |
| [Ne III] | 3869.84 | 11 468.93[c] | 149.9 ± 3.8 | 499 ± 13 |
| He I + H8 | 3890.17 | 11 527.64[c] | 95.3 ± 3.2 | 315 ± 11 |
| [Ne III] | 3968.53 | 11 761.36 | 64.3 ± 3.4 | 209 ± 11 |
| H7 | 3971.20 | 11 767.48 | 51.8 ± 1.7 | 168 ± 6 |
| Hδ | 4102.92 | 12 158.43 | 128.5 ± 2.7 | 403 ± 9 |
| Hγ | 4341.69 | 12 866.19 | 205.9 ± 1.3 | 610 ± 4 |
| Hβ | 4862.70 | 14 410.72[c] | 500.0 ± 0.9 | 1324 ± 2 |
| [O III] | 4960.29 | 14 700.41[c] | 669.5 ± 1.9 | 1739 ± 5 |
| [O III] | 5008.24 | 14 841.33[c] | 2357 ± 3.5 | 6066 ± 9 |
| He I | 5877.28 | 17 417.44 | 47.0 ± 5.2 | 104 ± 12 |
| Hα | 6564.63 | 19 453.85[c] | 1802.1 ± 0.6 | 3645 ± 1 |
| [N II] | 6585.42 | 19 513.96[c] | 58.1 ± 2.7 | 117 ± 5 |
| [S II] | 6718.29 | 19 910.44 | 156.8 ± 1.1 | 311 ± 2 |
| [S II] | 6732.67 | 19 951.76 | 102.7 ± 1.7 | 203 ± 3 |

[a]Rest-frame vacuum wavelengths.
[b]Emission-line flux in units of $10^{-18}$ erg cm$^{-2}$ s$^{-1}$. $f_{\rm obs}$ and $f_{\rm cor}$ correspond to the observed flux and that corrected for intrinsic reddening, respectively.
[c]Affected by telluric absorption lines.

where its lines are blended with the strong Fe II lines of the lensed galaxy's ISM.

## 2.3 SMACS J2031.8−4036 ID 1.1

Emission lines from this arc are listed in Table 3. The detected lines, excluding Lyα, give a flux-weighted average redshift of $z = 3.5073 \pm 0.0002$. At the low S/N per pixel in the UVB and VIS arms, we can only identify several Lyman forest absorption lines, and Si II λ1206 and S IV λλ1394, 1403 at $z = 3.5061 \pm 0.0013$. A detailed analysis of the absorption lines requires a spectrum with a higher S/N measured in the continuum, so we refrain from any detailed analysis of the present data. Again, the Lyα emission-line profile is double peaked, with a rest-frame EW of 20 Å (see Fig. 2),

**Table 3.** Emission lines from the SMACS J2031 arc.

| Line | $\lambda_{\rm r}$ [a] | $\lambda_{\rm obs}$ | $f_{\rm obs}$ [b] | $f_{\rm cor}$ [b] |
|---|---|---|---|---|
| Lyα | 1215.67 | 5480.80 | 173.7 ± 0.5 | 242 ± 1 |
| N IV] | 1486.50 | 6700.85 | 7.6 ± 0.9 | 10.1 ± 1.2 |
| O III] | 1660.81 | 7485.15 | 2.9 ± 0.6 | 3.8 ± 0.8 |
| O III] | 1666.15 | 7509.46 | 8.8 ± 0.7 | 11.5 ± 0.8 |
| [C III] | 1906.68 | 8594.04 | 12.0 ± 0.5 | 15.4 ± 0.6 |
| C III] | 1908.73 | 8603.54 | 8.4 ± 0.9 | 10.8 ± 1.2 |
| [O II] | 3727.09 | 16 800.18 | 14.4 ± 1.6 | 16.9 ± 1.9 |
| [O II] | 3729.88 | 16 811.01 | 15.5 ± 1.3 | 18.2 ± 1.5 |
| [Ne III] | 3869.84 | 17 442.96 | 14.8 ± 2.1 | 17.3 ± 2.5 |
| H I (H7) | 3971.20 | 17 898.76 | 6.0 ± 1.0 | 7.0 ± 1.2 |
| Hβ | 4862.70 | 21 917.47 | 37.7 ± 1.3 | 42.8 ± 1.5 |
| [O III] | 4960.29 | 22 357.68 | 61.9 ± 0.9 | 70.1 ± 1.0 |
| [O III] | 5008.24 | 22 573.68 | 205.2 ± 0.5 | 232 ± 0.6 |

[a]Rest-frame vacuum wavelengths.
[b]Emission-line flux in units of $10^{-18}$ erg cm$^{-2}$ s$^{-1}$. $f_{\rm obs}$ and $f_{\rm cor}$ correspond to the observed flux and that corrected for intrinsic reddening, respectively.
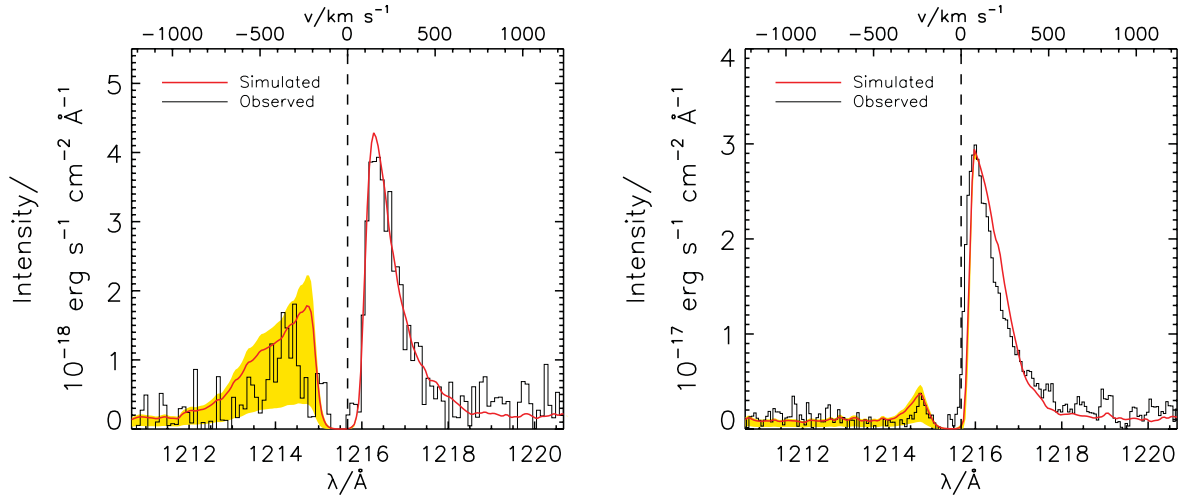
**Figure 2.** Observed (black) and fitted (red) spectra of the systems A31.1 (left) and M2031 (right). The yellow region shows the 68 per cent confidence interval due to absorption in the IGM.

and we will return in Section 4 with a more detailed treatment of this line.

At a low S/N we detect the semiforbidden N IV] $\lambda$1486 line which is rarely seen in high-$z$ galaxies, although a few detections of this line in emission are reported for lensed galaxies, for example cB58 (Pettini et al. 2000), the Lynx arc at $z = 3.3$ (Fosbury et al. 2003) and a galaxy at $z = 5.563$ (Raiter et al. 2010). When this line is detected, it can be interpreted as being caused by a large population of young and very hot, massive stars, but also an obscured active galactic nucleus (AGN) could be responsible for the ionization (Vanzella et al. 2010b). Since neither N V $\lambda\lambda$1238, 1242 nor He II $\lambda$1640 is detected, we exclude the possibility that the ionization is caused by an AGN (see table 1 in Binette et al. 2003). Hidden AGN like in radio galaxies typically display strong He II $\lambda$1640 lines (e.g. Villar-Martín et al. 1999).

# 3 PHYSICAL CONDITIONS FROM EMISSION LINES

All emission-line fluxes listed in Tables 1–3 are corrected for Galactic extinction using the dust maps in Schlegel, Finkbeiner & Davis (1998) along with an extinction curve in Fitzpatrick (1999) with $R_V = 3.1$. All the physical properties derived in this section are summarized in Table 4. When line ratios are considered, we do not apply any correction for slit losses and magnification factors, since we assume that the emission lines come from the exact same region.

## 3.1 Gas phase reddening

Any ratio of Balmer lines can be used to derive the reddening in the gas phase of the galaxies. In the absence of reddening, the

**Table 4.** Physical properties of sources with emission lines.

| Arc | A31.1 | M0304 | M2031 | Section |
|---|---|---|---|---|
| Magnification $\mu$ | $26.6 \pm 3.1$ | $42.0 \pm 8.0$ | $15.8 \pm 7.0$ | Paper I |
| $z_{em} - z_{abs}$ (km s$^{-1}$) | $95 \pm 131$ | $-10 \pm 55$ | $80 \pm 90$ | Paper I |
| $E(B-V)_{gas}$ (mag) | $0.37 \pm 0.28$ | $0.23 \pm 0.01$ | $0.03 \pm 0.33$ | 3.1 |
| $f_{esc,LL}$ | – | – | <11 per cent | 3.6 |
| $f_{esc,Ly\alpha}$ | 85 per cent | 0 per cent | 20–50 per cent | 4 |
| $T_e$ (K) | $21\,600 \pm 3000$ | $12\,900 \pm 900$ | $16\,100 \pm 300$ | 3.3 |
| $n_e$ [O II] (cm$^{-3}$) | $144 \pm 122$ | $81 \pm 8$ | $330 \pm 186$ | 3.3 |
| $n_e$ [C III] (cm$^{-3}$) | – | – | $2900 \pm 5000$ | 3.3 |
| $\log R_{23}$ | $0.85 \pm 0.05$ | $0.94 \pm 0.001$ | $0.91 \pm 0.02$ | 3.4.2 |
| $12 + \log(O/H)$ ($R_{23}$) | $7.63 \pm 0.10$ | $8.18 \pm 0.05$ | $7.74 \pm 0.03$ | Paper I |
| $Z/Z_{\odot, R_{23}}$ | 0.1 | 0.3 | 0.1 | Paper I |
| $12 + \log(O/H)$ (*O3N2*) | – | $8.04 \pm 0.01$ | – | Paper I |
| $12 + \log(O/H)$ (*Ne3O2*) | $7.85 \pm 0.15$ | $8.20 \pm 0.01$ | $7.56 \pm 0.11$ | Paper I |
| $12 + \log(O/H)$ (direct) | $7.69 \pm 0.13$ | $8.07 \pm 0.09$ | $7.76 \pm 0.03$ | 3.4.1 |
| $Z/Z_{\odot, direct}$ | 0.07 | 0.2 | 0.1 | |
| $\log U$ | $-2.1$ | $-2.8$ | $-2.1$ | 3.4.3 |
| $\log(C/O)$ | $-1.03 \pm 0.08$ | – | $-0.80 \pm 0.09$ | 3.4.3 |
| $\log(N/O)$ | – | $-1.64 \pm 0.05$ | – | 3.4.4 |

expected emission-line ratio is a function of the gas temperature and density. We adopt the values tabulated for temperatures $T = 10\,000$–$20\,000$ K and densities $n \sim 100 \, \mathrm{cm}^{-3}$ in Brocklehurst (1971). The choices of these values are based on the estimated gas temperature and density in Section 3.3.

To derive the gas phase reddening, $E(B-V)_{\mathrm{gas}}$, we use all of the Balmer line pairs available and calculate the weighted average, such that the reddening is determined by the Balmer line ratio with the smallest uncertainty. We assume an extinction curve derived for starburst galaxies (Calzetti et al. 2000), and the resulting reddening values are listed in Table 4. The reddening determined for M2031 is uncertain, and a value of zero is consistent with that determined from fitting the entire spectrum with stellar population models as demonstrated in Paper I.

## 3.2 Starburst/AGN ionization

The ionizing radiation from either AGN or recent formation of massive stars gives rise to strong emission lines in galaxies. Whether the narrow emission lines are caused by an AGN rather than a strong starburst is usually investigated through emission-line ratios, which are sensitive to the hard ionization from AGN. When only the strongest rest-frame optical emission lines can be detected, as is typically the case in high-redshift galaxies, the line ratios [O III]/H$\beta$ versus [N II]/H$\alpha$ can be used to distinguish the dominant ionizing source (Kewley & Dopita 2002). Among the galaxies analysed in this paper, only M0304 have all the relevant lines detected, and its line ratios are characteristic of star-forming galaxies.

In M2031, the C IV $\lambda\lambda$1548, 1550 lines are not detected to a level of $3 \times 10^{-18} \, \mathrm{erg \, cm^{-2} \, s^{-1}}$, so the ratio C IV $\lambda\lambda$1548, 1550/[C III]C III] $\lambda\lambda$1907, 1909 $< 0.15$ indicates a softer ionizing spectrum, while an AGN would cause a ratio of 2 as argued for the Lynx arc (Binette et al. 2003). The line ratio for A31.1 is C IV/C III] $= 0.65 \pm 0.71$ indicating a higher ionization parameter. In AGN, the lines N V $\lambda\lambda$1238, 1242 and He II $\lambda$1640 are expected to be strong, and since these lines are not detected in any of our spectra it suggests that the main contributor to the ionization is massive stars.

## 3.3 Gas temperatures and densities

Although [O III] $\lambda$4363, which is conventionally used for direct temperature measurements in low-redshift galaxies, is not detected in the M2031 source, the electron temperature can instead be derived directly from the O III] $\lambda\lambda$1661, 1666/[O III] $\lambda$5007 ratio as demonstrated for the Lynx arc (Villar-Martín et al. 2004). We use the NEBULAR package in IRAF (Shaw & Dufour 1995) to determine the gas phase temperatures and densities. From the oxygen line-flux ratio, we find $T_e = 16100 \pm 300$ K. The [C III], C III] $\lambda\lambda$1907, 1909 doublet can be used to derive densities. For M2031 we determine $n_e = 2900 \pm 5000 \, \mathrm{cm}^{-3}$ given that $T_e = 16100$ K. For the M0304 source, we also use the O III] $\lambda\lambda$1661, 1666/[O III] $\lambda$5007 ratio to derive the temperature and density directly, again after correcting the measured fluxes for reddening. The results are listed in Table 4.

Two different diagnostics can be used to derive the electron temperature for the Abell 1689 31.1 source. Using the O III] $\lambda\lambda$1661, 1666 lines gives $T_e = 26900 \pm 1000$ K, while the commonly used [O III] 4363 gives $T_e = 21600 \pm 3000$ K as determined iteratively using the equations in Aller (1984). Since the ratio from [O III] $\lambda$4363 over [O III] $\lambda\lambda$4959, 5007 is less affected by reddening, we chose to use the latter temperature measurement for further analysis of the oxygen abundance. The ratio of the [C III], C III] $\lambda\lambda$1907, 1909 $(1.9 \pm 0.2)$ doublet is unphysical at the $1.2\sigma$ level, as the maximum

allowed fraction is 1.65, however, the high value is consistent with a low electron density.

Since the [O II] $\lambda\lambda$3727, 3730 doublet is detected in all three galaxies, we can also use this to determine the electron density as listed in Table 4. The accurately measured electron densities from the medium resolution data of the three galaxies is similar to the densities in other lensed $z \sim 2$ galaxies where a range between a few 100 and a few 1000 $\mathrm{cm}^{-3}$ is common (Hainline et al. 2009; Wuyts et al. 2012).

## 3.4 Abundances

In this section we derive the integrated abundances of oxygen and carbon. These values are not dependent on magnification, because these parameters are derived from line-flux ratios rather than absolute values.

### 3.4.1 Direct ($T_e$) abundance measurements

Since we have measured the temperature directly for the sources, we can determine the oxygen abundance with direct temperature methods. We use the equations in Izotov et al. (2006) with the atomic data referenced in Stasińska (2005) to derive $O^{2+}/H^+$ and $O^+/H^+$. The sum of these two contributions gives the total oxygen abundance, when neglecting contributions from higher ionized stages, as is conventionally done. We take into account that the two different ions may reside in different zones of the H II region, and therefore have different electron temperatures. Since we do not detect the [O II] $\lambda\lambda$7320, 7331 lines in any of the spectra, we assume a relation between the temperatures $T(\mathrm{O\,II})$ and $T(\mathrm{O\,III})$ described by equation (14) in Izotov et al. (2006). The resulting oxygen abundances are listed in Table 4.

Using the temperature and densities determined in the section above, we calculate the total oxygen abundance for M2031. The derived uncertainty includes both the uncertainty from the emission-line fluxes, temperature and density. The contribution from singly ionized oxygen is $12 + \log(O^+/H^+) = 6.94 \pm 0.06$ and double ionized oxygen is $12 + \log(O^{2+}/H^+) = 7.69 \pm 0.02$. The sum gives the total oxygen abundance $12 + \log(O/H) = 7.76 \pm 0.03$, assuming that other oxygen ionizations states do not contribute.

For M0304 the contribution from single and double-ionized oxygen is $12 + \log(O^+/H^+) = 7.61 \pm 0.11$ and $12 + \log(O^{2+}/H^+) = 7.89 \pm 0.08$, respectively. The sum gives the total oxygen abundance $12 + \log(O/H) = 8.07 \pm 0.09$, again assuming that other oxygen ionization states do not contribute.

For Abell 1689 ID 31.1 the contribution from single- and double-ionized oxygen is $12 + \log(O^+/H^+) = 6.42 \pm 0.33$ and $12 + \log(O^{2+}/H^+) = 7.66 \pm 0.11$, respectively, and the total oxygen abundance is $12 + \log(O/H) = 7.69 \pm 0.13$ with the $T(\mathrm{O\,III})$ temperature determined from [O III] $\lambda$4363 in Section 3.3.

### 3.4.2 Strong-line diagnostics

In high-redshift galaxies temperature-sensitive lines are typically not detected. Instead one has to rely on the relations between strong emission-line ratios and the directly derived oxygen abundances. The ratio defined as $R_{23} = ([\mathrm{O\,II}] \, \lambda\lambda3727, \, 3730 + [\mathrm{O\,III}] \, \lambda\lambda4959, \, 5007)/\mathrm{H}\beta$ introduced by Pagel et al. (1979) is widely used, and its calibration relies either on photoionization models (e.g. McGaugh 1991; Kobulnicky, Kennicutt & Pizagno 1999; Kewley & Dopita 2002), or comparison with objects where direct

oxygen abundances are derived from temperature-sensitive lines (e.g. Alloin et al. 1979; Pilyugin & Thuan 2005; Nagao, Maiolino & Marconi 2006). The $R_{23}$ relation has two possible solutions with a high-metallicity and a low-metallicity branch. A degenerate solution can be avoided if other emission lines, such as [N II] $\lambda 6586$ or [Ne III] $\lambda 3869$, are detected (Denicoló, Terlevich & Terlevich 2002; Kewley & Dopita 2002; Pettini & Pagel 2004; Liang et al. 2006). Also the [O III] $\lambda 5007$/[O II] $\lambda 3727$ line ratio can be used to distinguish between the upper and lower branch of the $R_{23}$ calibrations (Nagao et al. 2006). Any strong emission-line diagnostics have large intrinsic scatters of $\sim 0.2$ dex, while various calibrations may differ by up to 0.7 dex relative to each other (Kewley & Ellison 2008), thereby making it difficult to compare objects from the literature.

The determinations of oxygen abundances using strong-line diagnostics were presented in Paper I, where we used [O II], [O III] or [Ne III] emission-line ratios to distinguish between the upper and lower branch of the $R_{23}$ calibration using the method in Pilyugin & Thuan (2005), the *O3N2* in Pettini & Pagel (2004) and *Ne3O2* in Nagao et al. (2006). For direct comparison, the derived oxygen abundances are reproduced in Table 4. In addition to the uncertainty of the abundance derived from the emission-line ratios, the calibrations themselves have an intrinsic scatter of $\sim 0.2$ dex, which must be taken into account when comparing the strong-line diagnostics with the direct measurements. In any case, it is encouraging that the strong-line calibration, in particular the one in Pilyugin & Thuan (2005), agrees very well with the direct oxygen abundances.

### 3.4.3 C/O abundance

The abundance ratio C/O increases with increasing oxygen abundance above 10 per cent solar. This trend is detected in halo stars, H II regions (Garnett et al. 1995) and in the integrated spectra of LBGs (Shapley et al. 2003). A subsolar C/O ratio arises when the production of O and C is dominated by Type II supernova explosions, while C can also be produced by intermediate-mass stars. Another explanation for the variation of the C/O ratio as a function of the oxygen abundance involves a metallicity dependence of the mass-loss rate for high-mass stars (Akerman et al. 2004).

Following the method in Erb et al. (2010) we use the ratio of O III] $\lambda\lambda 1661, 1666$ and [C III], C III] $\lambda\lambda 1907, 1909$ emission lines to determine the C/O abundance ratios. Since the ionization potentials for oxygen is higher than for carbon, $C^{3+}$ could be present in a medium with a high ionization parameter. The ionization parameter $U$ is defined as the ratio between the density of ionizing photons and the density of hydrogen atoms.

In the spectrum of M0304, the [C III], C III] $\lambda\lambda 1907, 1909$ doublet is not detected, even though it could have been, if the lines were as bright or brighter than O III] $\lambda\lambda 1661, 1666$. This is consistent with the note by Shapley et al. (2003) that the [C III], C III] lines appear to be stronger in LBGs with Ly$\alpha$ in emission.

Once we know the metallicity of a galaxy, the ratio of the emission lines [O III] $\lambda\lambda 4959, 5007$/[O II] $\lambda\lambda 3727, 3730$ can be used to determine the ionization parameter using the photoionization models and iterative equations in Kewley & Dopita (2002). The three galaxies all have $\log U$ between $-3$ and $-2$ as listed in Table 4. Similar high-ionization parameters have been measured for other gravitationally lensed galaxies (Hainline et al. 2009; Richard et al. 2011; Rigby et al. 2011), as well as changes in other emission-lines ratios in LBGs relative to local galaxies have been attributed to higher ionization parameters (Erb et al. 2006, 2010).

For an ionization parameter of $\log U \approx -2$, the dominant ionization level for both C and O are double ionized, and one can approximate $C/O \sim C^{2+}/O^{2+}$ (Erb et al. 2010), while at higher ionization parameters, an ionization correction factor (ICF) is necessary to include. Given the values of the ionization parameters in the three lensed galaxies, no ICFs are needed to derive the C/O ratio. For M2031 we calculate $\log(C^{2+}/O^{2+}) = -0.80 \pm 0.09$, while for Abell 1869 ID 31.1 we derive $\log(C^{2+}/O^{2+}) = -1.03 \pm 0.08$ based on the same emission-line ratio diagnostics. The results are listed in Table 4. Compared to the solar value $\log(C/O)_\odot = -0.26$ (Asplund et al. 2009), the observed ratios are subsolar. A decreasing C/O ratio with decreasing metallicity is a known property of unlensed LBGs (Shapley et al. 2003; Erb et al. 2010), and the low C/O ratios of the lensed galaxies measured here are consistent with their $\sim 0.1$ solar oxygen abundance.

The fact that we observe a low C/O ratio when the galaxy ages are very young [$\sim 4$ Myr according to spectral energy distribution (SED) models in Paper I], suggests that intermediate-mass stars have not contributed to the ISM in the galaxies. As concluded by Erb et al. (2010) a C/O value consistent with that observed in local metal-poor H II regions suggests that the carbon production in high-mass stars depends on their metallicities as predicted by either nucleosynthesis models (Weaver & Woosley 1993) or by mass loss from stellar winds (Maeder 1992).

### 3.4.4 N/O abundance

The nitrogen to oxygen ratio is an interesting parameter, because nitrogen provides a measure of the chemical enrichment history of a galaxy (see Petitjean, Ledoux & Srianand 2008). Nitrogen can be produces in two ways: a primary production from newly synthesized carbon via the CNO cycle, and a secondary production also from a CNO cycle, but with enhancement from a previous generation of stars that create additional carbon and oxygen.

To determine the N/O abundance ratio for M0304, which is the only source in the sample where [N II] $\lambda 6586$ is detected, we use the calibration of $\log(N^+/O^+)$ in Pagel et al. (1992). To account for the different ionization stages arising in different zones in the H II region, we convert the temperature measured for $T(O III)$ to $T(O II)$ as in Izotov et al. (2006). As argued by Thurston, Edmunds & Henry (1996), ionization models of low-metallicity gas show that $\log(N/O) \approx \log(N^+/O^+)$, and that an ionization correction factor is not necessary. For the M0304 source we find $\log(N/O) = -1.64 \pm 0.05$, which is below the plateau seen in low-metallicity H II regions in dwarf and irregular galaxies (van Zee & Haynes 2006). The observed (N/O) ratio is more similar to the ratios observed in the more metal-rich ($\sim 0.1$ solar) damped Ly$\alpha$ systems (Petitjean et al. 2008; Pettini et al. 2008; Battisti et al. 2012), and considerably below the solar level of $\log(N/O)_\odot = -0.86$ (Asplund et al. 2009). This subsolar (N/O) ratio suggests that the galaxy, like in high-redshift damped Ly$\alpha$ absorbers, has only experienced the primary production of nitrogen from the CNO cycle, and cannot have had a large population of stars forming earlier because these would have increased the nitrogen level. This is consistent with a young age of $\sim 60$ Myr based on stellar population model fits in Paper I.

### 3.5 Lyman $\alpha$ escape fraction

Two sources, M2031 and A1689 ID 31.1 have double-peaked Ly$\alpha$ emission lines, which is not uncommon as it is seen in 30 per cent of LBGs at $z = 2$–3 (Kulas et al. 2012), and up to 50 per cent of Ly$\alpha$

emitters (Yamada et al. 2012). Only few lensed galaxies studied in detail to date are also strong Lyα emitters (Fosbury et al. 2003; Quider et al. 2009; Bayliss et al. 2010), so the present data allow for a more in depth analysis including constraints from the rest-frame optical emission lines. The escape fraction can be determined from the observed Balmer emission lines relative to the observed Lyα line flux. Under the assumption of a case B recombination scenario, and zero extinction, we find that the escape fraction of Lyα photons from M2031 is 20 per cent, and 4 or 85 per cent for the A1689 31.1 arc before and after correction for an intrinsic reddening of $E(B - V) = 0.37$.

At comparable redshifts, the comparison of galaxies UV luminosity to their Lyα emission lines have revealed a median Lyα escape fraction of 29 per cent, where any value between 0 and 100 per cent is possible (Blanc et al. 2011). Similarly to our calculations, comparisons of the flux from Hα and Lyα lines for both $z \sim 0.3$ galaxies (Atek et al. 2009) and a few $z \sim 2$ galaxies (Hayes et al. 2010) indicate a large range of Lyα escape fractions from 0 to 100 per cent. There is a tendency that larger escape fractions are found for galaxies with smaller reddenings (Hayes et al. 2010; Blanc et al. 2011), but only when the Lyα emission lines are not corrected for the intrinsic reddening, similar to what we find for the two Lyα emitters in this study.

### 3.6 Lyman limit escape fraction

The M2031 source has a sufficiently high redshift that we can derive an upper limit on the escape fraction bluewards of the Lyman limit. In the region 3800–4100 Å, corresponding to a rest-frame wavelength of ∼900 Å, the average flux measured in the extracted 1D spectrum after binning by a factor of 50 in the dispersion is ($1 \pm 5$) $\times$ $10^{-20}$ erg cm$^{-2}$ s$^{-1}$ Å$^{-1}$, while the observed flux at the rest frame 1500 Å is ($2.3 \pm 0.3$) $\times$ $10^{-18}$ erg cm$^{-2}$ s$^{-1}$ Å$^{-1}$. The relative escape fraction at these wavelengths needs to be corrected for the absorption in the intergalactic medium (IGM; e.g. Inoue, Iwata & Deharveng 2006; Boutsia et al. 2011):

$$f_{\text{esc,LL}} = \frac{(F_{1500}/F_{900})_{\text{int}}}{(f_{1500}/f_{900})_{\text{obs}}} \exp\left(-\tau_{900}^{\text{IGM}}\right),$$

where $T = \exp(-\tau_{900}^{\text{IGM}})$ is the transmission in the IGM at the rest frame 900 Å. The intrinsic fraction of the flux densities $(F_{1500}/F_{900})_{\text{int}}$ is model dependent, and we determine the ratio from the best-fitting spectral template in Paper I to be 1.44. Since we do not find evidence for significant intrinsic reddening, this value is not corrected for extinction. From the observed ratio and an optical depth of the IGM at $z = 3.5$ due to the Lyman series (Madau 1995) giving a transmission of 0.2 at $\lambda = 900(1 + 3.5)$ Å, we derive an upper limit for the escape fraction $f_{\text{esc,LL}} < 0.031 \pm 0.025$, or <3.0 ± 2.5 per cent. However, the IGM transmission varies significantly along different sight lines due to the random occurrence of intervening Lyman limit systems, and at $z \sim 3.5$ the IGM transmission just bluewards of the Lyman limit is $T = 0.3 \pm 0.2$ based on numerical simulations (Inoue & Iwata 2008). Accordingly, our limit to the escape fraction is less constrained: $f_{\text{esc,LL}} < 11$ per cent.

In a sample of 14 LBGs at $z \sim 3$ Shapley et al. (2006) found a significant escape fraction in two galaxies implying an average escape fraction of 14 per cent. However, because spatial offsets between the galaxy emission in the rest-frame Lyman continuum and at rest-frame optical wavelengths have been measured, the large escape fraction could be contaminated by lower redshift interlopers. Consequently, Vanzella et al. (2010a) find that LBGs at $z \sim 4$ have upper limit of $f_{\text{esc,LL}} < 5$–20 per cent. A stacked spectrum of 11

LBGs at $z = 3.3$ gave an upper limit of <5 per cent (Boutsia et al. 2011), albeit dominated by a couple of bright LBGs, which may not be representative for the average high-redshift galaxy population. Shapley et al. (2006) and Boutsia et al. (2011) use STARBURST99 templates (Leitherer et al. 1999), with an intrinsic flux ratio of three between 1500 and 900 Å. A larger flux ratio is the result of an older stellar population, which in turn depends on the assumed star formation history. If we assume the same intrinsic ratio (i.e. 3), the corresponding limit on the escape fraction derived for the M2031 galaxy would be a factor of 2 higher, i.e. $f_{\text{esc,LL}} < 22$ per cent.

Even though lensing significantly boosts the signal from faint galaxies such that we can detect very small fluxes at rest frame 900 Å for the M2031 source, which has an intrinsic UV luminosity of $9L^*$ determined from the SED fits in Paper I, we may have to look for intrinsically much fainter galaxies ($<0.1L^*$) that are expected to dominate the escaping UV flux at high redshifts. Future observations of gravitationally lensed faint galaxies offer an opportunity for determining $f_{\text{esc,LL}}$ (Vanzella et al. 2012).

## 4 MODELLING THE LYα EMISSION LINES

To infer the physical conditions governing the two systems for which Lyα emission is detected, we undertake a series radiative transfer (RT) simulations, with the aim of fitting synthetic spectra to the observed ones. For this purpose, we apply the three-dimensional Lyα scattering code MOCALATA (Laursen, Razoumov & Sommer-Larsen 2009a), including the effects of dust (Laursen, Sommer-Larsen & Andersen 2009b). In the following, the basics of the simulations are outlined.

The galaxies are modelled as spherical conglomerations of gas existing in two phases: warm, chiefly neutral clouds of relatively high neutral hydrogen density, dispersed in a hotter and more ionized intercloud medium (ICM). The ICM density, as well as the number density of clouds, decreases exponentially with distance from the centre. Additionally, the systems are surrounded by a spherical shell of outflowing gas.

Densities, temperatures and velocity fields are assigned to cells in a Cartesian grid. The grid has a base resolution of $128^3$ cells, with cells constituting the edge of clouds being refined recursively into eight cells, to make clouds more spherical. In addition, Lyα photons are also emitted from the centre and out with a luminosity which decreases exponentially with radius. A photon is traced as it scatters its way out of the galaxy on individual hydrogen atoms, constantly changing direction and frequency, or, alternatively, is absorbed by dust. To obtain good statistics for the spectrum, a total of ∼$10^5$ photons are emitted.

At the redshifts of the two emitters ($z = 1.8$ and 3.5 for A31.1 and M2031, respectively), the IGM is ionized to a high degree. Nevertheless, a fraction of the photons blueward of the Lyα line may still be scattered out of the line of sight by diffuse neutral gas clouds in the circumgalactic medium. This effect is modelled in a statistical way following Laursen, Sommer-Larsen & Razoumov (2011).

In addition to matching the observed spectra, the preferred model should also be consistent with the SFRs obtained in Paper I, as well as with the escape fractions inferred from comparing the integrated Lyα and Hα fluxes. Under these constraints, and considering the large number of free parameters in the model, rather than searching the full parameter space as has been done previously for a shell-only model of four parameters, including gas and dust column density, temperature and expansion velocity (Verhamme et al. 2008; Schaerer et al. 2011), a series of simulations is conducted, changing

the various input parameters until a satisfactory fit is obtained. This approach has been demonstrated to be able to match simultaneously a broad range of observables for a single system (Noterdaeme et al. 2012).

As an 'initial' model, we make use of the few observational constraints we have at hand. Since we have measured the metallicities of the two systems (0.07 and 0.10 solar for A31.1 and M2031, respectively), this parameter is held fixed in the simulation to limit the already high number of free parameters.

Assuming an Small Magellanic Cloud (SMC) extinction law and a dust-to-metal ratio similar to the local Universe (which is thought to be approximately valid even at high redshift; see e.g. Pettini et al. 1997; Pei, Fall & Hauser 1999; Savaglio, Fall & Fiore 2003), the dust density is calculated. The MoCaLaTA code can model the dust as either Large Magellanic Cloud (LMC) or SMC dust. We choose SMC dust, as the young stellar population of the SMC may be expected to match more closely those of the observed galaxies, but note that the difference between various extinction laws is of minor importance; over the narrow spectral region of the Ly$\alpha$ line, the dust cross-section is almost flat, and indeed a comparison study in Laursen et al. (2009b) of the two dust models reveals a change in escape fractions at the $\sim$1 per cent level only. Furthermore, the fact that the blue components of the spectra are significantly smaller than the red ones, albeit still visible, is a hint of modest outflow velocities. Finally, for the temperatures we assume typical values of the three phases in the model: $10^4$, $2 \times 10^4$ and $10^5$ K for the clouds, the ICM and the expanding shell, respectively.

### 4.1 Best-fitting models

Fig. 2 shows the best-fitting models to the observed spectra, given the constraints. The synthetic spectra have been scaled by an SFR of 0.8 and 4.5 M$_\odot$ yr$^{-1}$, respectively, which is consistent with the values found in Section 3. Moreover, the escape fractions were found to be 0.87 and 0.56, respectively. While the former matches perfectly the value found for A31.1, the latter is somewhat higher than the $\sim$0.20 found for M2031, although due to the rather large uncertainty on the fluxes, it is not inconsistent. Table 5 summarizes the final parameter values used for the models.

**Table 5.** Galaxy model values.

| Parameter | A31.1 | M2031 |
|---|---|---|
| Galaxy radius | 1 kpc | 1 kpc |
| Number of clouds | 80 | 200 |
| Cloud radii | 20 pc | 20 pc |
| Cloud temperature | $10^4$ K | $10^4$ K |
| Cloud density[a] | 2.5 cm$^{-3}$ | 100 cm$^{-3}$ |
| Metallicity | 0.07 Z$_\odot$ | 0.1 Z$_\odot$ |
| Cloud velocity dispersion | 50 km s$^{-1}$ | 10 km s$^{-1}$ |
| Central ICM density[a] | $7.5 \times 10^{-2}$ cm$^{-3}$ | $3 \times 10^{-4}$ cm$^{-3}$ |
| ICM density[a] scale length | 0.4 kpc | 1 kpc |
| ICM temperature | $5 \times 10^4$ K | $5 \times 10^4$ K |
| Shell radius | 1 kpc | 1 kpc |
| Shell expansion velocity | 60 km s$^{-1}$ | 110 km s$^{-1}$ |
| Shell column density[a] | $3 \times 10^{18}$ cm$^{-2}$ | $10^{18}$ cm$^{-2}$ |
| Shell temperature | $5 \times 10^5$ K | $5 \times 10^5$ K |
| Ly$\alpha$ emission scale length | 0.1 kpc | 0.25 kpc |
| Intrinsic Ly$\alpha$ EW | 40 Å | 20 Å |

[a]All densities refer to *neutral* hydrogen only.

Note that the models are perfectly scalable: radii of 1 and 2 kpc have been assumed for A31.1 and M2031, respectively; however, the exact same spectra and escape fractions would emerge from models with twice the radius, but with all densities a factor of 4 smaller, and scale lengths and cloud radii doubled.

As mentioned in Section 2, the asymmetric profile is characteristic of an expanding ISM. However, the fact that we *do* see the blue peaks in both spectra tells us that the typical outflow velocities must be quite low. For a homogeneous medium, the blue peak vanishes already at $V_{out} \sim 100$ km s$^{-1}$ for a broad range of column densities (e.g. Verhamme, Schaerer & Maselli 2006). For an inhomogeneous medium, since the photons blueward of the line may find low-density paths out of the galaxy, higher velocities may be allowed with the blue peak still visible.

The outflows of the two models that match the observed spectra best are 60 and 110 km s$^{-1}$ for A31.1 and M2031, respectively. This is consistent with the values inferred from comparing the redshifts of the absorption and emission lines (see Table 4). Although the rather large uncertainties in the latter values make them consistent with zero as well, we consider it likely that the two emitters in fact do exhibit outflow. In principle, foreground diffuse H I clouds could also cause a decreased blue peak. At the given redshifts the IGM is likely to be highly ionized. However, its clumpy nature could in principle cause absorption nevertheless. In Fig. 2, the yellow region marks the 68 per cent confidence level of the Ly$\alpha$ emission line, *after* being transmitted through the IGM. Indeed, the expected impact of the IGM is rather low.

Most observed Ly$\alpha$ emitters exhibit an asymmetric line profile with the blue peak missing. However, with sufficient spectral resolution it seems that the fraction of Ly$\alpha$ emitters where the blue peak is still visible is quite large (20–50 per cent; Kulas et al. 2012; Yamada et al. 2012).

It is important to keep in mind that we do not claim that the model galaxies must be a realistic representation of the real galaxies. Many processes shape the Ly$\alpha$ line, and these are to some extend degenerate. Nevertheless, it is striking that it is possible to match the lines under the restrictions set by the other observables such as metallicity and SFR.

The higher SFR and metallicity of M2031 relative to A31.1 hints at the former being more evolved than the latter. This interpretation is backed up by the results of the simulations; the higher number of clouds and the larger density contrast between clouds and ICM imply a more fragmented ISM. The shallower density gradient could then be caused by the enhanced star formation 'inflating' the galaxy, while the higher wind velocity is a natural consequence of a more vigorous feedback.

## 5 SUMMARY

We have measured the oxygen abundance using direct $T_e$ methods for three galaxies at $z = 1.8$, 2.0 and 3.5, respectively. The direct oxygen abundance measurements are in agreement with those derived from the conventional $R_{23}$ ratio using the diagnostics calibration in Pilyugin & Thuan (2005). This proves that the strong-line diagnostics are in fact useful to determine oxygen abundances in high-redshift galaxies, as the temperature-sensitive lines for field galaxies are almost always below the detection limit even on 8-m telescopes.

In addition, we have measured the C/O and N/O ratios for the three galaxies, and argue that their ratios are consistent with the general trend of subsolar metal ratios for low-metallicity galaxies,

and in particular for young galaxies where contributions from either nitrogen or carbon from older stars have not yet occurred.

We have modelled the emission-line profiles in two strong Ly$\alpha$ emitting galaxies using the constraints (SFR, reddening, escape fractions and metallicity) obtained from the analysis of their spectra. The relatively small inferred expansion velocities of the neutral gas shells correspond to the small velocity offsets seen in absorption and rest-frame emission lines. The observed absorption and emission-line redshifts show that the velocity offsets are consistent with zero at the $1\sigma$ confidence level, but are also consistent with the small shell expansion velocities (60 and 110 km s$^{-1}$, respectively) found in the radiative transfer simulations. Compared to more massive LBGs with higher SFRs we observe a smaller velocity offset between the absorption and Ly$\alpha$ emission wavelengths. To develop our understanding how galaxy outflows are related to the SFRs and escape of Ly$\alpha$ photons, it would be interesting to expand the sample and verify if the trend of decreasing velocity offset with increasing Ly$\alpha$ EW observed for LBGs (Shapley et al. 2003) is present also in Ly$\alpha$ emitters with much higher EWs.

Recent studies of Ly$\alpha$ emitters have shown that the absorption lines are more difficult to detect at progressively larger Ly$\alpha$ EWs, even when stacking the data from many emitters (Berry et al. 2012). Gravitational lensing is the only means to obtain medium- to high-resolution spectroscopic data of high-EW Ly$\alpha$ emitters (Diehl et al. 2009; Quider et al. 2009; Bayliss et al. 2010). The A31.1 source, with an EW of 40 Å, does not appear to have strong absorption lines, but the faint continuum and low S/N of the spectrum prevent a more detailed analysis besides the strongest Si II lines at 1260, 1264 and 1526 Å. Since 1 h integration time per target was used in this study, we conclude that it would be possible to investigate the detailed physics of a strong Ly$\alpha$ emitter with a few more hours integration time on a large telescope.

Future observations of strong lensing clusters, such as the *HST*/Cluster Lensing And Supernova survey with Hubble (CLASH; Postman et al. 2012), may reveal more potentially interesting lensed high-redshift sources with steep UV slopes and high surface brightness regions. These could be the best targets to locate and investigate the interstellar absorption lines in strong Ly$\alpha$ emitting galaxies. These galaxies are also the prime candidates to find other strong UV lines such that abundances of several species could be determined by direct methods. With such observations, we could constrain better chemical evolution models of high-redshift galaxies.

## REFERENCES

Akerman C. J., Carigi L., Nissen P. E., Pettini M., Asplund M., 2004, A&A, 414, 931
Allam S. S., Tucker D. L., Lin H., Diehl H. T., Annis J., Buckley-Geer E. J., Frieman J. A., 2007, ApJ, 662, L51
Aller L. H., ed., 1984, Astrophys. Space Sci. Libr. Vol. 112, Physics of Thermal Gaseous Nebulae. Reidel, Dordrecht
Alloin D., Collin-Souffrin S., Joly M., Vigroux L., 1979, A&A, 78, 200
Asplund M., Grevesse N., Sauval A. J., Scott P., 2009, ARA&A, 47, 481
Atek H., Kunth D., Schaerer D., Hayes M., Deharveng J. M., Östlin G., Mas-Hesse J. M., 2009, A&A, 506, L1
Battisti A. J. et al., 2012, ApJ, 744, 93
Bayliss M. B., Wuyts E., Sharon K., Gladders M. D., Hennawi J. F., Koester B. P., Dahle H., 2010, ApJ, 720, 1559
Berry M. et al., 2012, ApJ, 749, 4
Bian F. et al., 2010, ApJ, 725, 1877
Binette L., Groves B., Villar-Martín M., Fosbury R. A. E., Axon D. J., 2003, A&A, 405, 975
Blanc G. A. et al., 2011, ApJ, 736, 31
Boutsia K. et al., 2011, ApJ, 736, 41
Brocklehurst M., 1971, MNRAS, 153, 471
Cabanac R. A., Valls-Gabaud D., Jaunsen A. O., Lidman C., Jerjen H., 2005, A&A, 436, L21
Calzetti D., Armus L., Bohlin R. C., Kinney A. L., Koornneef J., Storchi-Bergmann T., 2000, ApJ, 533, 682
Christensen L., D'Odorico S., Pettini M., Belokurov V., Evans N. W., Kellogg M., Vernet J., 2010, MNRAS, 406, 2616
Christensen L. et al., 2012, MNRAS, 427, 1953 (this issue) (Paper I)
Denicoló G., Terlevich R., Terlevich E., 2002, MNRAS, 330, 69
Dessauges-Zavadsky M., D'Odorico S., Schaerer D., Modigliani A., Tapken C., Vernet J., 2010, A&A, 510, A26
Dessauges-Zavadsky M., Christensen L., D'Odorico S., Schaerer D., Richard J., 2011, A&A, 533, A15
Diehl H. T. et al., 2009, ApJ, 707, 686
D'Odorico S. et al., 2006, Proc. SPIE, 6269, 626933
Ebeling H., Edge A. C., Henry J. P., 2001, ApJ, 553, 668
Erb D. K., Shapley A. E., Pettini M., Steidel C. C., Reddy N. A., Adelberger K. L., 2006, ApJ, 644, 813
Erb D. K., Pettini M., Shapley A. E., Steidel C. C., Law D. R., Reddy N. A., 2010, ApJ, 719, 1168
Fitzpatrick E. L., 1999, PASP, 111, 63
Fosbury R. A. E. et al., 2003, ApJ, 596, 797
Garnett D. R., Skillman E. D., Dufour R. J., Peimbert M., Torres-Peimbert S., Terlevich R., Terlevich E., Shields G. A., 1995, ApJ, 443, 64
Hainline K. N., Shapley A. E., Kornei K. A., Pettini M., Buckley-Geer E., Allam S. S., Tucker D. L., 2009, ApJ, 701, 52
Hayes M. et al., 2010, Nat, 464, 562
Holden B. P. et al., 2001, AJ, 122, 629
Inoue A. K., Iwata I., 2008, MNRAS, 387, 1681
Inoue A. K., Iwata I., Deharveng J.-M., 2006, MNRAS, 371, L1
Izotov Y. I., Stasińska G., Meynet G., Guseva N. G., Thuan T. X., 2006, A&A, 448, 955
Kewley L. J., Dopita M. A., 2002, ApJS, 142, 35
Kewley L. J., Ellison S. L., 2008, ApJ, 681, 1183
Kobulnicky H. A., Kennicutt R. C., Jr, Pizagno J. L., 1999, ApJ, 514, 544
Kulas K. R., Shapley A. E., Kollmeier J. A., Zheng Z., Steidel C. C., Hainline K. N., 2012, ApJ, 745, 33
Lara-López M. A. et al., 2010, A&A, 521, L53
Laursen P., Razoumov A. O., Sommer-Larsen J., 2009a, ApJ, 696, 853
Laursen P., Sommer-Larsen J., Andersen A. C., 2009b, ApJ, 704, 1640
Laursen P., Sommer-Larsen J., Razoumov A. O., 2011, ApJ, 728, 52
Leitherer C. et al., 1999, ApJS, 123, 3
Liang Y. C., Yin S. Y., Hammer F., Deng L. C., Flores H., Zhang B., 2006, ApJ, 652, 257
Limousin M. et al., 2007, ApJ, 668, 643
Lin H. et al., 2009, ApJ, 699, 1242
McGaugh S. S., 1991, ApJ, 380, 140
Madau P., 1995, ApJ, 441, 18
Maeder A., 1992, A&A, 264, 105
Mannucci F., Cresci G., Maiolino R., Marconi A., Gnerucci A., 2010, MNRAS, 408, 2115
Nagao T., Maiolino R., Marconi A., 2006, A&A, 459, 85
Noterdaeme P. et al., 2012, A&A, 540, A63

Osterbrock D. E., 1989, Astrophysics of Gaseous Nebulae and Active Galactic Nuclei. University Science Books, Mill Valley, CA

Pagel B. E. J., Edmunds M. G., Blackwell D. E., Chun M. S., Smith G., 1979, MNRAS, 189, 95

Pagel B. E. J., Simonson E. A., Terlevich R. J., Edmunds M. G., 1992, MNRAS, 255, 325

Pei Y. C., Fall S. M., Hauser M. G., 1999, ApJ, 522, 604

Petitjean P., Ledoux C., Srianand R., 2008, A&A, 480, 349

Pettini M., Pagel B. E. J., 2004, MNRAS, 348, L59

Pettini M., King D. L., Smith L. J., Hunstead R. W., 1997, ApJ, 478, 536

Pettini M., Steidel C. C., Adelberger K. L., Dickinson M., Giavalisco M., 2000, ApJ, 528, 96

Pettini M., Rix S. A., Steidel C. C., Adelberger K. L., Hunt M. P., Shapley A. E., 2002, ApJ, 569, 742

Pettini M., Zych B. J., Steidel C. C., Chaffee F. H., 2008, MNRAS, 385, 2011

Pettini M. et al., 2010, MNRAS, 402, 2335

Pilyugin L. S., Thuan T. X., 2005, ApJ, 631, 231

Postman M. et al., 2012, ApJS, 199, 25

Quider A. M., Pettini M., Shapley A. E., Steidel C. C., 2009, MNRAS, 398, 1263

Quider A. M., Shapley A. E., Pettini M., Steidel C. C., Stark D. P., 2010, MNRAS, 402, 1467

Raiter A., Fosbury R. A. E., Teimoorinia H., 2010, A&A, 510, A109

Richard J., Jones T., Ellis R., Stark D. P., Livermore R., Swinbank M., 2011, MNRAS, 413, 643

Rigby J. R., Wuyts E., Gladders M. D., Sharon K., Becker G. D., 2011, ApJ, 732, 59

Savaglio S., Fall S. M., Fiore F., 2003, ApJ, 585, 638

Schaerer D., Hayes M., Verhamme A., Teyssier R., 2011, A&A, 531, A12

Schlegel D. J., Finkbeiner D. P., Davis M., 1998, ApJ, 500, 525

Shapley A. E., Steidel C. C., Pettini M., Adelberger K. L., 2003, ApJ, 588, 65

Shapley A. E., Steidel C. C., Pettini M., Adelberger K. L., Erb D. K., 2006, ApJ, 651, 688

Shaw R. A., Dufour R. J., 1995, PASP, 107, 896

Stark D. P., Swinbank A. M., Ellis R. S., Dye S., Smail I. R., Richard J., 2008, Nat, 455, 775

Stasińska G., 2005, A&A, 434, 507

Steidel C. C., Giavalisco M., Pettini M., Dickinson M., Adelberger K. L., 1996, ApJ, 462, L17

Swinbank A. M., Bower R. G., Smith G. P., Wilman R. J., Smail I., Ellis R. S., Morris S. L., Kneib J.-P., 2007, MNRAS, 376, 479

Teplitz H. I. et al., 2000, ApJ, 533, L65

Thurston T. R., Edmunds M. G., Henry R. B. C., 1996, MNRAS, 283, 990

van Zee L., Haynes M. P., 2006, ApJ, 636, 214

Vanzella E. et al., 2010a, ApJ, 725, 1011

Vanzella E. et al., 2010b, A&A, 513, A20

Vanzella E. et al., 2012, MNRAS, 424, L54

Verhamme A., Schaerer D., Maselli A., 2006, A&A, 460, 397

Verhamme A., Schaerer D., Atek H., Tapken C., 2008, A&A, 491, 89

Vernet J. et al., 2011, A&A, 536, A105

Villar-Martín M., Fosbury R. A. E., Binette L., Tadhunter C. N., Rocca-Volmerange B., 1999, A&A, 351, 47

Villar-Martín M., Cerviño M., González Delgado R. M., 2004, MNRAS, 355, 1132

Weaver T. A., Woosley S. E., 1993, Phys. Rep., 227, 65

Wuyts E., Rigby J. R., Sharon K., Gladders M. D., 2012, ApJ, 755, 73

Yamada T., Matsuda Y., Kousai K., Hayashino T., Morimoto N., Umemura M., 2012, ApJ, 751, 29

Yuan T., Kewley L. J., 2009, ApJ, 699, L161

This paper has been typeset from a TEX/LATEX file prepared by the author.